A puffy polar planet: the low density, hot Jupiter TOI-640 b is on a polar orbit

Knudstrup, E.; Albrecht, S.H.; Gandolfi, D.; Marcussen, M.L.; Goffo, E.; Serrano, L.M.; ... ; Eylen, V. van

A&A 671, A164 (2023)
https://doi.org/10.1051/0004-6361/202245301

Astronomy & Astrophysics

A puffy polar planet

The low density, hot Jupiter TOI-640 b is on a polar orbit⋆

Emil Knudstrup[1], Simon H. Albrecht[1], Davide Gandolfi[2], Marcus L. Marcussen[1], Elisa Goffo[2,3], Luisa M. Serrano[2], Fei Dai[4,5], Seth Redfield[6], Teruyuki Hirano[7,8], Szilárd Csizmadia[9], William D. Cochran[10], Hans J. Deeg[11,12], Malcolm Fridlund[13,14], Kristine W. F. Lam[9], John H. Livingston[7,8,15], Rafael Luque[16], Norio Narita[17,7,11], Enric Palle[11,12], Carina M. Persson[14], and Vincent Van Eylen[18]

(Affiliations can be found after the references)

Received 26 October 2022 / Accepted 28 January 2023

ABSTRACT

TOI-640 b is a hot, puffy Jupiter with a mass of $0.57 \pm 0.02\ M_J$ and radius of $1.72 \pm 0.05\ R_J$, orbiting a slightly evolved F-type star with a separation of $6.33^{+0.07}_{-0.06}\ R_\star$. Through spectroscopic in-transit observations made with the HARPS spectrograph, we measured the Rossiter-McLaughlin effect, analysing both in-transit radial velocities and the distortion of the stellar spectral lines. From these observations, we find the host star to have a projected obliquity of $\lambda = 184 \pm 3°$. From the TESS light curve, we measured the stellar rotation period, allowing us to determine the stellar inclination, $i_\star = 23^{+3}_{-2}°$, meaning we are viewing the star pole-on. Combining this with the orbital inclination allowed us to calculate the host star obliquity, $\psi = 104 \pm 2°$. TOI-640 b joins a group of planets orbiting over stellar poles within the range 80°−125°. The origin of this orbital configuration is not well understood.

Key words. planet-star interactions – techniques: photometric – techniques: spectroscopic – planets and satellites: gaseous planets

1. Introduction

Before 1992, the only planetary system we knew of was the Solar System. The neat and ordered structure we see in the Solar System therefore formed the architectural drawing for planetary formation and evolution. However, with the detection of the first exoplanet, it immediately became clear that this schematic does not apply to all systems. For instance, the very first exoplanet discovered is orbiting a pulsar (Wolszczan & Frail 1992), the first exoplanet around a Sun-like star is a Jupiter-sized planet on a ∼4 d orbit (Mayor & Queloz 1995), and some systems harbour planets on wildly eccentric orbits (e.g. Cochran et al. 2008). The type of host stars, the orbital separations, and eccentricities are just some of the parameters indicating how different exoplanet systems can be from the Solar System.

Another parameter is the angle between the stellar spin axis of the host and the orbital axis of the planet, the spin-orbit angle, or the obliquity ψ[1]. At $7.155 \pm 0.002°$ (Beck & Giles 2005), the obliquity of the Solar System is relatively low. In contrast, in exoplanet systems, measurements of ψ, or its projection on the sky λ, or the difference along the line of sight between orbital and stellar spin, display a large variety of values. The configurations range from well aligned to (moderately) misaligned, and there are even retrograde systems (see e.g. the review by Albrecht et al. 2022, and references therein). There is also a curious trend reported by Albrecht et al. (2021); systems for which ψ has been measured are either consistent with good alignment or the planets orbit over the stellar poles. This preponderance of perpendicular planets was not evident from λ measurements alone, as without additional knowledge, meaningful inferences about ψ cannot be drawn from λ measurements (Fabrycky & Winn 2009).

Here we aim to measure the host star obliquity in the TOI-640 system discovered and characterised by Rodriguez et al. (2021). To this end, we make use of the Rossiter-McLaughlin (RM) effect, an apparent distortion of the stellar line shapes caused by a transiting body blocking part of the rotating stellar disk. The RM effect allows us to measure the sky-projected obliquity, λ. To measure the stellar inclination, we use light curves from the Transiting Exoplanet Survey Satellite (TESS; Ricker et al. 2015). Together with knowledge of the orbital inclination, we can infer the spin-orbit angle of our target system.

The paper is organised as follows. In Sect. 2, we present the observations, both photometric and spectroscopic. Section 3 presents the determination of the obliquity of the host star. Our new radial velocities (RVs) and photometry allow us to also update a number of other system parameters. We discuss these together with our result on the spin-orbit angle in Sect. 4 before giving our conclusions in Sect. 5.

2. Observations

2.1. TESS photometry

Table 1 lists a selection of parameters determined by Rodriguez et al. (2021). These authors presented TESS data of TOI-640 from Sectors 6 and 7 taken with a cadence of 30 min. Additional TESS photometry has become available since then, as the system was observed again in Sectors 33 and 34. This time the system was observed with a cadence of 2 min. Figure A.1 displays the TESS data from all four sectors.

⋆ Based on observations made with the ESO-3.6 m telescope at La Silla Observatory under programme 106.21TJ.001.

[1] We note that here we are discussing the obliquity of the host star and not the planet. In this article, we use the terms obliquity and spin-orbit angle interchangeably.

Table 1. Literature system parameters.

Parameter	Value
Stellar mass, $M_\star$ ($M_\odot$)	$1.536^{+0.069}_{-0.076}$
Stellar radius, $R_\star$ ($R_\odot$)	$2.082^{+0.064}_{-0.058}$
Effective temperature, $T_{\rm eff}$ (K)	6460^{+130}_{-150}
Surface gravity, $\log g$ (dex)	$3.987^{+0.030}_{-0.036}$
Metallicity (dex), [Fe/H]	$0.072^{+0.085}_{-0.076}$
Age, τ (Gyr)	$1.99^{+0.55}_{-0.40}$
Proj. rotational velocity, $v \sin i_\star$ (km s^{-1})	6.1 ± 0.5
Macroturbulence, $v_{\rm mac}$ (km s^{-1})	6.32 ± 1.37
Orbital period, P (days)	5.0037775(48)
Planet-to-star radius ratio, $R_{\rm p}/R_\star$	$0.08738^{+0.00091}_{-0.00086}$
Semi-major axis / star radius, $a/R_\star$	$6.82^{+0.22}_{-0.24}$
Velocity semi-amplitude, K (m s^{-1})	78 ± 14
Impact parameter, b	$0.8763^{+0.0063}_{-0.0067}$
Eccentricity, e	$0.050^{+0.054}_{-0.035}$
Planet radius, $R_{\rm P}$ ($R_{\rm J}$)	$1.771^{+0.060}_{-0.056}$
Planet mass, $M_{\rm P}$ ($M_{\rm J}$)	0.88 ± 0.16

Notes. Selected stellar, orbital, and planetary parameters from Rodriguez et al. (2021).

We downloaded and reduced the TESS data utilising the python package `lightkurve` (Lightkurve Collaboration 2018). First, we corrected for noise induced by the motion of the spacecraft and removed scattered light using the `RegresssionCorrector` routine. The result is shown in the top panel of Fig. A.1. To exclude outliers, we then (temporarily) removed the transits from the planet using the best-fitting transit parameters, which were determined by fitting the light curve iteratively. The resulting light curves are shown in the middle panel of Fig. A.1, where we also overplotted a Savitzky-Golay (Savitzky & Golay 1964) filter to (again temporarily) smooth the light curve. Points more than 5σ away from the smoothed light curves were rejected (19 out of 36 918 points were removed). The bottom panel of Fig. A.1 displays the unfiltered light curves with outliers excluded, but with the transits re-injected. This is the light curve we use in the analysis for determining the projected spin-orbit angle in Sect. 3.1, whereas we use the light curve with the transits removed for determining the rotation period in Sect. 3.2.

2.2. HARPS spectroscopy

To measure the RM effect, we observed a transit of TOI-640 b that occurred during the night 2022 February 26 UT using the High-Accuracy Radial Velocity Planetary Searcher (HARPS; Mayor et al. 2003) as part of our observing programme 106.21TJ.001 (PI: Gandolfi). HARPS is mounted at the European Southern Observatory (ESO)-3.6 m telescope at La Silla, Chile. We obtained 22 spectra on the transit night of which 4 were acquired before the beginning of ingress, 14 during transit, and 4 after egress. The average exposure time was 900 s and the median signal-to-noise ratio (S/N) per pixel at 550 nm was 45. We continued to monitor the system using HARPS until 2022 November 23 UT covering a total time span of 271 days with an additional 40 radial velocities. For these monitoring observations, the exposure times varied between 1200 s and 1500 s depending on sky conditions, and the median S/N was 50. The extracted RVs, their associated errors, and photometric mid-times are shown in Fig. A.2 and listed in Tables A.1 and A.2. Figure 1 shows the HARPS RVs centred on the mid-transit time, focusing in on the RM effect.

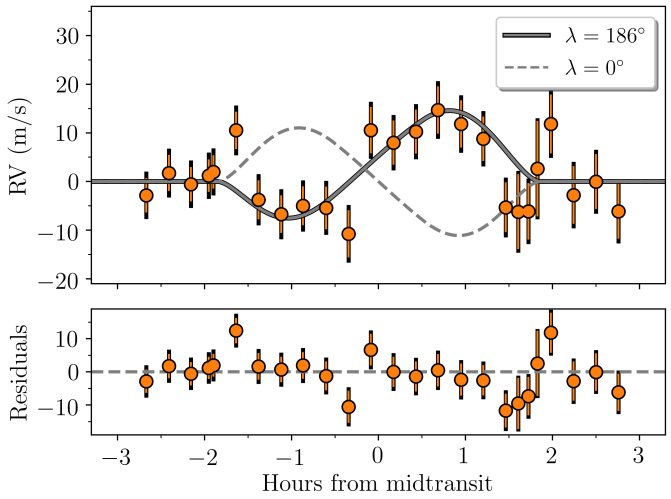

Fig. 1. Rossiter-McLaughlin effect as seen from HARPS RVs centred around the mid-transit time after subtracting the Keplerian motion induced by the planet. The grey line shows the RM effect with the best-fitting (retrograde) model as the solid line and an aligned model as the dashed line. The error bars include the jitter term from our MCMC added in quadrature, shown as the black extension.

3. Stellar obliquity

In this section, we first conduct a joint fit of both the photometric and spectroscopic data to measure the projected spin-orbit angle of TOI-640 (Sect. 3.1). We then determine the stellar inclination along the line of sight making use of TESS photometry (Sect. 3.2) and through the use of an empirical relation (Sect. 3.3). Together with the orbital inclination, we can then determine the stellar obliquity (Sect. 3.4). Our results for ψ as well as other system parameters are then discussed in Sect. 4.

3.1. Projected obliquity from the Rossiter-McLaughlin effect

Spectrally resolved stellar lines observed during transits (or eclipses) will display distortions; this is known as the RM effect. For example, in a system where the projections of the stellar spin axis and the orbital axis of the planet are aligned (low projected obliquity), a transiting planet would first hide sections of the approaching stellar surface. A distortion of the lines with a negative velocity (relative to the current RV of the star) will appear. During later phases of the transit, further areas of the stellar surface with positive radial velocities (redshifted) will be hidden from view. This distortion can also be sensed as anomalous RVs during transits. In this case, first positive and later negative RVs are observed. However, if the spin-orbit angle is larger than 90° (a retrograde configuration) then the time evolution of the distortion and RVs is reversed. From a glance at Figs. 1 and 2, it appears as if the orbit of TOI-640 b is indeed retrograde.

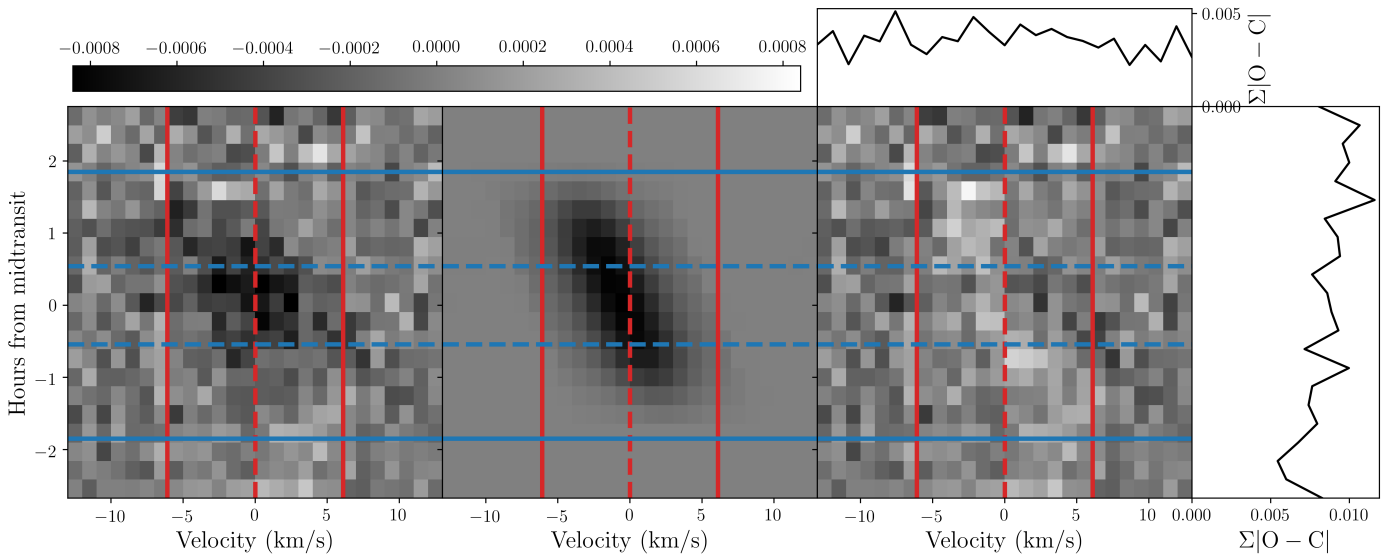

Fig. 2. Planetary shadow. *Left*: distortion of the stellar absorption lines as seen for our observations with HARPS taken on the transit night. The vertical solid lines denote $\pm v \sin i_\star$, and the vertical dashed line is at $v = 0$ km s^{-1}. The horizontal dashed lines mark the points of second and third contact, which is when the planet is found completely within the stellar disk, and the solid lines denote the first and fourth contact points, where the planetary and stellar disk start to overlap. *Middle*: best-fitting model of the distortion. *Right*: residuals from subtracting the best-fitting model from the data. The horizontal bar on top shows the strength of the signal.

Our approach to a quantitative analysis of the RM effect is similar to the analyses performed in Knudstrup & Albrecht (2022), Knudstrup et al. (2022), and we briefly summarise it here. Also, the following procedure is included in the python package ~~tracit~~[2], which was used in these latter two publications.

We performed a joint fit of the photometric and spectroscopic data. Specifically, we performed two different analyses of the spectroscopic data. First, we analysed the anomalous RVs obtained during the transit. We then performed a second analysis where we do not use the RVs during transit but the underlying distortions of the line shapes, or the so-called planet shadow. We did this to check for consistency between the different measurement approaches (Albrecht et al. 2007). In both cases, we also made use of the orbital RV measurements and the TESS photometry and we applied the same priors.

When determining λ through the anomalous RVs, we used the RVs obtained from the HARPS Data Reduction Software (DRS; Lovis & Pepe 2007). When analysing the planetary shadow, we used the cross-correlation functions (CCFs) obtained from the DRS as a proxy for the stellar absorption lines. With HARPS' resolution of $R = 120\,000$, the point spread function (PSF) has a full width at half maximum (FWHM) of 2.5 km s^{-1} or an equivalent dispersion of $\sigma \approx 1$ km s^{-1}. The CCFs delivered by the HARPS DRS are over-sampled with a datum every 0.25 km s^{-1}. To account for this, we interpolated the CCFs onto a grid with a resolution of 1 km s^{-1}. This is the same approach as taken in Knudstrup & Albrecht (2022) and similar to the approach taken by Cegla et al. (2016), for instance, where every fourth datum in the grid is sampled.

The relevant parameters in both approaches are the orbital period P, mid-transit time T_0, planet-to-star radius ratio $R_p/R_\star$, scaled semi-major axis $a/R_\star$, orbital inclination i, RV semi-amplitude K, orbital eccentricity e, argument of periastron ω, projected stellar obliquity λ, projected stellar rotation speed $v \sin i_\star$, macro-turbulence ζ, micro-turbulence ξ, systemic velocity γ, and two sets of separate pairs of quadratic limb-darkening coefficients c_1, c_2, for TESS and HARPS.

We applied Gaussian priors on $v \sin i_\star$ (from Table 1), as well as ζ and ξ estimated from the relations in Doyle et al. (2014) and Bruntt et al. (2010), respectively, using the parameters in Table 1. The Gaussian priors for the limb-darkening coefficients were obtained from the tables by Claret et al. (2013) and Claret (2018) for HARPS and TESS, respectively. Uncertainties of 0.1 were assumed. Uniform priors were applied for all other parameters.

To model the RM effect for the RVs, we used the code by Hirano et al. (2011), while we used the formulation in Albrecht et al. (2007, 2013b) to model the planetary shadow. We modelled the TESS data using the `batman` package (Kreidberg 2015). This was done with the inclusion of Gaussian process (GP) regression – utilising the library `celerite` (Foreman-Mackey et al. 2017) – to characterise the photometric noise (stellar and instrumental). For our GP, we used a Matérn-3/2 kernel, which is characterised by two hyperparameters; the amplitude, A, and the timescale, τ. We sampled the posterior distribution for the parameters through Markov chain Monte Carlo (MCMC) sampling using the code `emcee` (Foreman-Mackey et al. 2013). In our MCMC, we stepped in $\sqrt{e}\cos\omega$ and $\sqrt{e}\sin\omega$ as opposed to stepping in e and ω directly. For the limb-darkening parameters, we stepped in the sum of the coefficients while keeping the difference fixed. Furthermore, we stepped in $\cos i$ instead of i, allowing us to apply a flat prior assuming an isotropic spin distribution a priori. All stepping parameters and priors are listed in Tables 2 and A.3. Our likelihood is defined as

$$\log \mathcal{L} = -0.5 \sum_{i=1}^{N} \left[\frac{(O_i - C_i)^2}{\sigma_i^2} + \log 2\pi\sigma_i^2 \right] + \sum_{j=1}^{M} \mathcal{P}_j \,, \tag{1}$$

where N indicates the total number of data points from photometry and RVs. C_i represents the model corresponding to the observed data point O_i, and $\mathcal{P}_j$ is the prior on the jth parameter.

Finally, before starting the joint spectroscopic photometric MCMC runs, we performed simple minimisations on each of the three data types. We then added 'jitter' terms in quadrature to

[2] https://tracit.readthedocs.io/en/latest/

Table 2. MCMC results.

Parameter	Name	Prior	RV Value	Shadow Value
		Stepping parameters		
P	Period (days)	$\mathcal{U}$	$5.003777^{+0.000002}_{-0.000003}$	5.003777 ± 0.000003
T_0	Mid-transit time (BTJD)	$\mathcal{U}$	1459.7413 ± 0.0003	1459.7414 ± 0.0003
$R_p/R_\star$	Planet-to-star radius ratio	$\mathcal{U}$	$0.0851^{+0.0003}_{-0.0004}$	$0.0850^{+0.0004}_{-0.0003}$
$a/R_\star$	Semi-major axis to star radius ratio	$\mathcal{U}$	$6.33^{+0.07}_{-0.06}$	$6.32^{+0.08}_{-0.07}$
K	Velocity semi-amplitude (m s^{-1})	$\mathcal{U}$	50.1 ± 1.0	$50.0^{+1.1}_{-1.2}$
$\cos i$	Cosine of inclination	$\mathcal{U}$	$0.143^{+0.002}_{-0.003}$	$0.143^{+0.002}_{-0.003}$
$\sqrt{e}\cos\omega$		$\mathcal{U}$	$0.00^{+0.06}_{-0.07}$	0.02 ± 0.07
$\sqrt{e}\sin\omega$		$\mathcal{U}$	$0.06^{+0.03}_{-0.06}$	$0.07^{+0.03}_{-0.07}$
λ	Projected obliquity (°)	$\mathcal{U}$	184 ± 3	189 ± 8
$v \sin i_\star$	Projected rotational velocity (km s^{-1})	$\mathcal{N}(6.1,0.5)$	5.9 ± 0.4	6.2 ± 0.4
ζ	Macro-turbulence (km s^{-1})	$\mathcal{N}(6.65,1.0)$	$6.6^{+0.9}_{-0.8}$	7.3 ± 0.8
ξ	Micro-turbulence (km s^{-1})	$\mathcal{N}(1.52,1.0)$	1.7 ± 0.8	$1.6^{+0.8}_{-0.9}$
$\gamma_{\rm HARPS}$	Systemic velocity HARPS (m s^{-1})	$\mathcal{U}$	40525.4 ± 0.7	$40525.6^{+0.9}_{-0.8}$
$\sigma_{\rm HARPS}$	Jitter HARPS (m s^{-1})	$\mathcal{U}$	3.9 ± 0.7	4.2 ± 1.0
		Derived parameters		
e	Eccentricity	–	<0.013 (1σ)	<0.016 (1σ)
ω	Argument of periastron (°)	–	87^{+50}_{-55}	74^{+35}_{-63}
i	Inclination (°)	–	$81.79^{+0.16}_{-0.12}$	$81.78^{+0.18}_{-0.14}$
b	Impact parameter	–	$0.904^{+0.005}_{-0.007}$	$0.904^{+0.006}_{-0.008}$
T_{41}	Total transit duration (hours)	–	$3.696^{+0.018}_{-0.019}$	$3.696^{+0.019}_{-0.020}$
T_{21}	Time from 1st to 2nd contact (hours)	–	1.32 ± 0.04	$1.31^{+0.04}_{-0.05}$
		Physical parameters		
$T_{\rm eq}$	Equilibrium temperature (K)	–	1816 ± 39	1817 ± 39
R_p	Planet radius (R_J)	–	1.72 ± 0.05	1.72 ± 0.05
M_p	Planet mass (M_J)	–	0.57 ± 0.02	0.57 ± 0.02
ρ_p	Planet density (g cm^{-3})	–	0.138 ± 0.013	0.138 ± 0.013
ρ_p	Planet density (ρ_J)	–	0.104 ± 0.010	0.104 ± 0.010

Notes. The median and highest posterior density at a confidence level of 0.68. $\mathcal{U}$ or $\mathcal{N}$ denotes that a uniform or a Gaussian prior, respectively, was applied during the run. Barycentric TESS Julian Date (BTJD) is defined as BJD-2457000.0, BJD being the Barycentric Julian Date.

the respective uncertainties until reduced χ^2 of 1 were obtained. This was done in an attempt to ensure proper weighting between spectroscopic and photometric data.

The observed RVs and the best-fitting model are shown in Fig. 1, and the results are presented in the fourth column of Table 2. The observed shadow and best-fitting model can be seen in Fig. 2 with the results presented in the fifth column of Table 2. For both runs, RVs and shadow, we present the nuisance parameters in Table A.3. We show the correlation plot for $v \sin i_\star$ and λ for both runs in Fig. 3. An extended correlation plot for more parameters can be found in Fig. A.3.

The amplitude of the RM signal (relative to the noise) seen in Figs. 1 and 2 is modest; nevertheless the uncertainties in our λ measurements are comparably low. This is because the large impact parameter of $0.904^{+0.005}_{-0.007}$ acts as a lever. Even a small change in λ leads to a transit chord passing over stellar surface areas with substantially different rotational RVs.

The λ measurement from the analysis of the RVs comes out to $184 \pm 3°$, and has a lower uncertainty than the measurement from the planet shadow $189 \pm 8°$. This is because the overall line width – mainly governed by $v \sin i_\star$ relative to the width of the distortion – is only modest (Fig. 2). A larger $v \sin i_\star$ value would have reversed the situation as it would have lead to a more localised distortion (planet shadow) in the lines (Albrecht et al. 2022). At the same time, a larger $v \sin i_\star$ leads to a larger RV uncertainty. These two advantages of analysing the line distortions relative to analysing the RVs vanish for lower $v \sin i_\star$. In addition, the shadow measurement requires alignment and normalisation of the CCFs (Knudstrup & Albrecht 2022). This takes away some of the predictive power from the CCFs as these additional 'hyper parameters' (not to be confused with the GP hyper parameters) have to be determined (Albrecht et al. 2013a). This process is similar to the 'Hyperplane Least Squares' method described and tested by Bakos et al. (2010). Here, for the case of

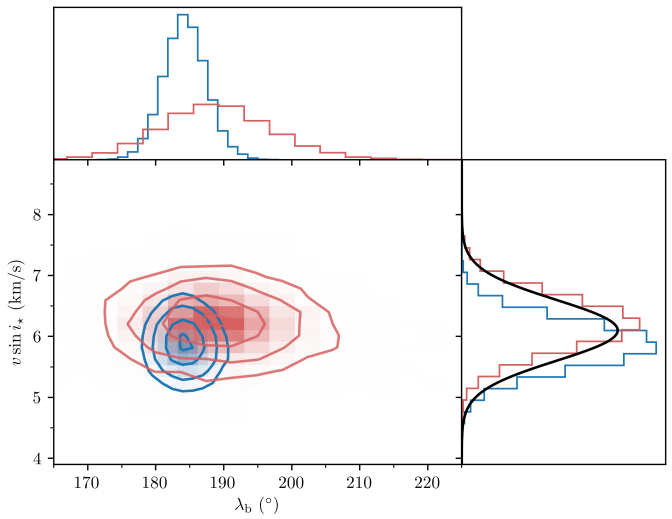

Fig. 3. 2D histograms. The correlation between λ and $v \sin i_\star$ from our MCMCs. Blue shows the results from our RV run, while red is from the shadow run.

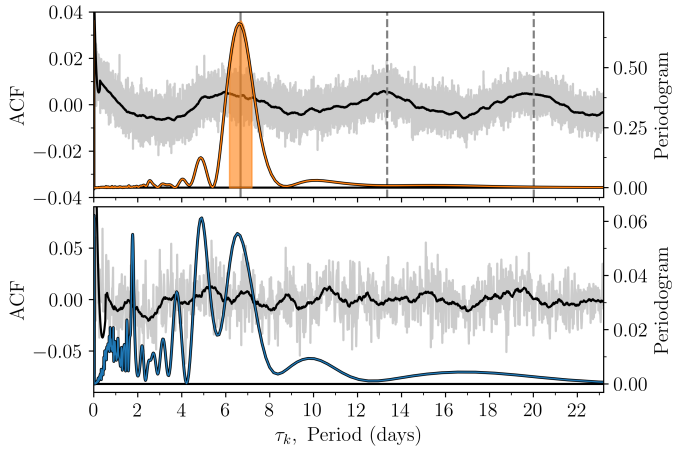

Fig. 4. Autocorrelation function. The ACFs are shown as the grey curves with a smoothed version in black. The (coloured) periodogram is calculated from the smoothed ACF. The y-axis on the left (right) is for the ACF (periodogram). *Top*: the 2 min cadence ACF with the corresponding periodogram. The vertical grey line denotes the measured rotation period, and the dashed lines are integer values of this value. Shown as the shaded area is the confidence interval for the rotation period. *Bottom*: the 30 min cadence ACF.

TOI-640, we therefore use the values obtained via the analysis of the anomalous RVs moving forward.

Up to this point, we have determined λ, the projected spin-orbit angle. Next, we determine the stellar inclination, $i_\star$, using two different methods. Together with the orbital inclination, this allows us to determine the obliquity, ψ.

3.2. Stellar inclination from TESS photometry

The starting point for our first inclination measurement is the rotation period of the star, $P_{\rm rot}$, as determined from TESS photometry in Fig. A.1. We used the light curves in the middle, where the transits have been removed by the best-fitting transit model. We measured the rotation period using the autocorrelation method (e.g. McQuillan et al. 2013). We do this by calculating the autocorrelation function (ACF) for the 2 min cadence and 30 min cadence separately. We then smoothed the ACF using a Savitzky-Golay filter from which we calculated the Generalised Lomb-Scargle (GLS; Lomb 1976; Scargle 1982) periodogram.

While we can clearly identify a single peak (at around 6.7 days) in the periodogram for the 2 min cadence case, we also see some additional features most likely associated with momentum dumps of the spacecraft causing 'jumps' in the light curves. An example of how these jumps affect the ACF and periodogram is illustrated in the third column of Fig. 2 in McQuillan et al. (2013). We therefore applied a Savitzky-Golay filter to the light curves to remove these jumps. The resulting ACFs and periodograms are shown in Fig. 4. Evidently, the rotation is detected much more clearly for the 2 min cadence case, but it is also apparent in the 30 min cadence. We therefore proceeded with the results from the 2 min cadence periodogram.

We fitted a Gaussian to the peak in the periodogram to get an estimate of the period and the uncertainty. From this, we got a rotation period of $P_{\rm rot} = 6.7 \pm 0.6$ d, which we can use with $R_\star = 2.082 \pm 0.061\ R_\odot$ to calculate the stellar inclination from

$$\sin i_\star = \frac{P_{\rm rot} v \sin i_\star}{2\pi R_\star}. \tag{2}$$

We followed the approach in Masuda & Winn (2020) to properly calculate $i_\star$ from Eq. (2), meaning we accounted for the fact that v and $v \sin i_\star$ are not independent. From this, we get a rotation speed at the equator of $v = 14 \pm 2$ km s^{-1} and subsequently a stellar inclination of $i_\star = 23^{+3\circ}_{-2}$.

3.3. Stellar inclination from the empirical relation

In the second approach, we used the results from Louden et al. (2021), who investigated the obliquities of *Kepler* planets around hot stars. This required that the authors determine the v distribution of a sample of control stars without detected transiting planets. From that sample, they obtained a relation between the mean rotation velocity of a star as a function of the effective temperature. We can use this relation with the $T_{\rm eff}$ from Table 1 to calculate $i_\star$. We obtain $i_\star = 20^{+6}_{-9}$ deg.

Using this relation from Louden et al. (2021) would not be appropriate in the case of tidal spin-up in which tides raised on the star by the planet change the rotation of the star. This effect has been suggested to take place in some hot Jupiter systems (e.g. Brown 2014; Maxted et al. 2015; Yee et al. 2023). How effectively the planet can raise tides on the star is especially dependent on the separation, but also on the mass ratio (see e.g. Zahn 1977). A useful metric to assess whether tides are effectively raised is given by $(M_{\rm p}/M_\star)(R_\star/a)^3$ which for TOI-640 b is 1.4×10^{-6}, meaning that tides should not play an important role and suggesting that the use of the relation from Louden et al. (2021) is warranted. For our final result for the spin-orbit angle, we use the stellar inclination measurement from the previous section and simply note here that the two inclination measurements from this and the above section are consistent.

3.4. Stellar obliquity

As we now have values for $i_\star$, i, and λ, we can use

$$\cos\psi = \sin i_\star \sin i \cos\lambda + \cos i_\star \cos i \tag{3}$$

to calculate the spin-orbit angle, ψ. Here we used our distributions for λ and i from our MCMC (Table 2), and we drew normally distributed values from $i_\star = 23 \pm 2.5°$ (determined above in Sect. 3.2) for each of these draws. There are two

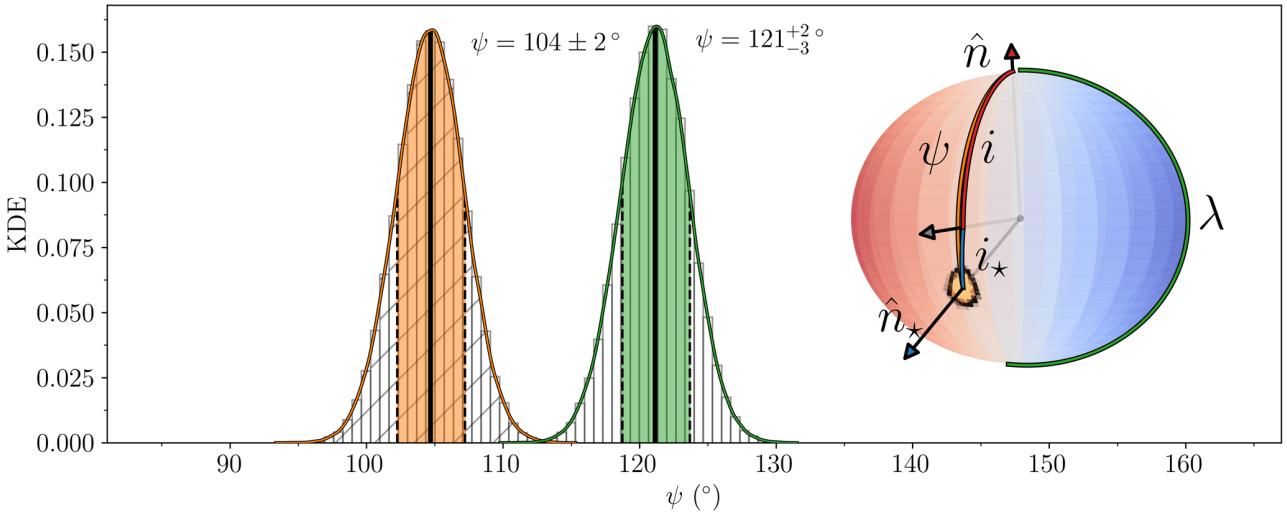

Fig. 5. Obliquity distributions. The histograms are the distributions for ψ calculated from the rotation period in Sect. 3.2 with the KDE overplotted as the solid lines. The coloured areas are the confidence intervals with the medians shown as the black lines. The orange distribution corresponds to using the orbital inclination, i, directly from our posteriors and the green is $i - 180°$. On the sphere, we only show the "orange" distribution for ψ as the heatmap. We do this for a fixed value of i (in terms of how the sphere is oriented). The sphere is colour coded according to the perceived movement of the stellar disk with the approaching (receding) side in blue (red) for an observer along the line of sight, which is denoted by the grey arrow.

solutions. This is because our observations cannot distinguish between $i_\star$ and $180° - i_\star$; they can also not distinguish between (i, λ) and $(180° - i, -\lambda)$. In the case of an exactly edge-on orbit ($i = 90°$), the two solutions would collapse into one. The resulting histogram and kernel density estimation (KDE) are shown in orange and green in Fig. 5. We find $104 \pm 2°$ or $121^{+2}_{-3}{}^\circ$ for the spin-orbit angle. If the orbital inclination were exactly edge on ($i = 90°$), then our result for the obliquity would be $\psi = 113^{+3}_{-2}{}^\circ$.

If we had not been able to determine the stellar rotation period from the TESS light curve then we could have attempted to determine ψ from the inclination measurement obtained in Sect. 3.3. In that case, we would have found a spin-orbit angle of $101^{+5}_{-9}{}^\circ$ or $117^{+6}_{-8}{}^\circ$. The resulting histograms and KDEs for this approach are shown in Fig. A.4. The results are consistent between the two inclination estimates. We report the spin-orbit angle estimated from the rotation period for the conventional orientation (i not $180° - i$) as our final result, which we find to be $\psi = 104 \pm 2°$.

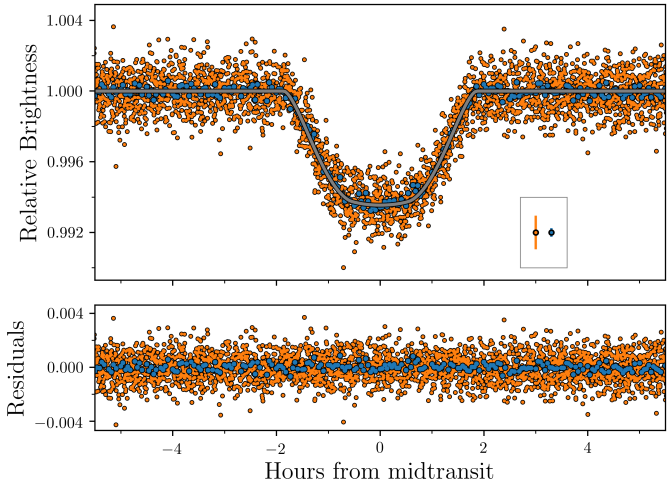

Fig. 6. TESS transits of TOI-640 b. TESS photometry phase folded to the period from Table 2 and centred on the transit. As in Fig. A.1, blue and orange points are the 30 and 2 min cadence data, respectively. The points with error bars in the box are not data, but illustrate the typical errors for the data. The data shown here have been detrended with the GP (white line in Fig. A.1). The grey curve is the best-fitting light curve.

4. Discussion

4.1. Refined parameters for TOI-640 b

From our joint fit of the photometry and the in- and out-of-transit RVs, in addition to λ, we also provide new values for other system parameters and list them in Table 2. Some of these new determinations differ significantly from previous determinations and we discuss these first before we discuss the implications of our obliquity measurement.

In Fig. 6 we show the phase-folded TESS photometry with the best-fitting transit model. We find a radius of $1.72 \pm 0.05\ R_J$ for TOI-640 b. This is consistent with the value of $1.777^{+0.060}_{-0.056}\ R_J$ from Rodriguez et al. (2021), but is slightly more precise owing to the additional TESS photometry and increased cadence. While we find consistent results for the radius, with $0.57 \pm 0.02\ M_J$ we find a roughly 2σ difference in mass from the value reported in Rodriguez et al. (2021) of $0.88 \pm 0.16\ M_J$.

We find a value of $0.906^{+0.007}_{-0.009}$ for the impact parameter, differing by roughly 3σ from $0.8763^{+0.0063}_{-0.0067}$ obtained by Rodriguez et al. (2021). This then leads to a significant difference in the results for $a/R_\star$ (our $6.31^{+0.09}_{-0.07}$ versus $6.82^{+0.22}_{-0.24}$) which is correlated with the impact parameter ($b = \cos i \frac{a}{R_\star}$). These differences in the photometric solutions may be caused by Rodriguez et al. (2021) using the then available TESS photometric data from Sectors 6 and 7 together with ground-based photometry, while we have access to Sectors 6 and 7 and Sectors 33 and 34 and do not use additional ground-based data. This discrepancy might also be caused by the difference in how the light curves have been de-trended. Furthermore, it could be due to the spectroscopic transit data as the analysis of RM data can drive the

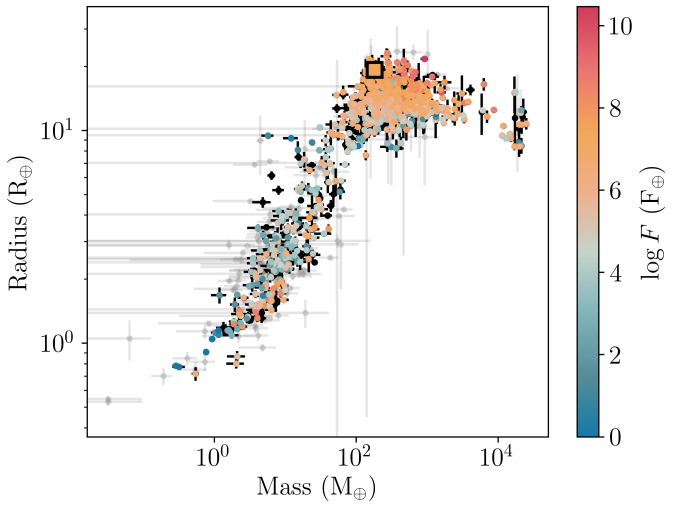

Fig. 7. Mass–radius diagram. Here we show planets from the TEPCat catalogue of 'well-studied transiting planets' (as of October 2022; Southworth 2011, https://www.astro.keele.ac.uk/jkt/tepcat/allplanets-noerr.html). Grey dots are measurements with uncertainties larger than 30%, while black and coloured dots have smaller uncertainties. Points are colour coded according to the insolation, F, for those objects where it can be calculated. TOI-640 b is shown as the large square.

result on b (Albrecht et al. 2022). We investigated whether or not the results for b are consistent between the different TESS observing epochs. For this, we determined b only on photometric data; first on Sectors 6 and 7 only and then on Sectors 33 and 34 only, obtaining $b = 0.917^{+0.006}_{-0.005}$ and $b = 0.911^{+0.006}_{-0.005}$, respectively. The values are consistent with each other and our final result. We note here that given the high impact parameter for the transit of TOI-640 b, any change in orbital inclination caused by for example nodal precession (see e.g. Szabó et al. 2012; Johnson et al. 2015; Watanabe et al. 2020, 2022; Stephan et al. 2022) may be picked up by future photometric (TESS) observations.

As noted in Rodriguez et al. (2021), TOI-640 b is an inflated planet. The lower mass but similar radius we find here compared to Rodriguez et al. (2021) makes it an even puffier planet with a density of 0.138 ± 0.013 g cm^{-3}. Comparing TOI-640 b to the literature, it is one of the largest and puffiest planets, but is not isolated in the mass–radius diagram as seen in Fig. 7. The puffiness is most likely due to the rather high insolation it receives.

Finally, we investigated the light curve to see if we could see any effects of gravity darkening. However, the star does not seem to be rotating fast enough to detect this effect in the TESS photometry available.

4.2. The polar orbit of TOI-640 in context

Albrecht et al. (2021) derived ψ for a subset of planetary systems for which λ measurements were available. Of the 57 systems where ψ could be determined, these authors found 38 systems to be well-aligned and 18 systems misaligned in the interval between 80° and 125°, meaning that the misaligned systems are not isotropically distributed. Rather there is a tendency for planets to be orbiting the poles of the star.

With a value for ψ of $104 \pm 2°$ (or $121^{+2}_{-3}°$), TOI-640 joins this preponderance of perpendicular planets. Given the effective temperature of the star of 6460^{+130}_{-150} K, which is relatively hot in this context, one might even say that our measurement of $\psi = 104 \pm 2°$ is not particularly surprising, seeing as the 'polar-to-aligned ratio' seems to increase with effective temperature. This might be an echo of the often larger projected obliquities found for stars with effective temperatures above 6250 K (Winn et al. 2010), as well as lower $v \sin i_\star$ for spectral types of F or earlier Schlaufman (2010).

Further measurements of ψ have recently been made. Fig. 8 shows MASCARA-1 b ($\psi = 72.1^{+2.5}_{-2.4}°$; Hooton et al. 2022), GJ 3470 b ($\psi = 95^{+9}_{-8}°$; Stefánsson et al. 2022), KELT-7 b ($\psi = 12.4 \pm 11.7°$; Tabernero et al. 2022), and TOI-640 b ($\psi = 104 \pm 2°$) along with the measurements presented in Albrecht et al. (2021). Evidently, these new measurements follow the tendency of polar orbiting planets, where especially for hot stars harbour polar orbiting planets.

However, when discussing the sample of polar planets, it is important to keep in mind the various different selection effects that might play a role. For a classic example, see Fig. 1 by Winn et al. (2010) and for a more recent discussion on selection effects related to spin-orbit angle measurements, see Albrecht et al. (2022). In this context, we note that we first selected TOI-640 as a system for which RM measurements, employing HARPS, are likely to result in a conclusive answer concerning λ. We only started analysing the TESS light curves to establish whether or not we were able to determine the stellar rotation period from these light curves after the RM measurements had been taken.

As to why planets should show a tendency to travel over stellar poles, Albrecht et al. (2021) briefly discuss four mechanisms, which we simply list here as (1) tidal dissipation (Lai 2012; Rogers & Lin 2013; Anderson et al. 2021), (2) Von Zeipel-Kozai-Lidov cycles (Fabrycky & Tremaine 2007), (3) secular resonance crossing (Petrovich et al. 2020), and (4) magnetic warping (Foucart & Lai 2011; Lai et al. 2011; Romanova et al. 2021). Another recent proposal was presented by Vick et al. (2023), who highlight that a binary companion (and its influence on the obliquity during disk dissipation) combined with subsequent Kozai-Lidov cycles might also produce polar orbits. While these mechanisms might be able to explain parts of the observed distribution, they do not seem to be able to fully reproduce the observations individually. It would be interesting to increase the sample size and expand the parameter space to try to decipher whether or not these mechanisms work in tandem in different types of systems harbouring different types of planets.

5. Conclusions

Here we present in-transit spectroscopic measurements for the hot Jupiter TOI-640 b. These measurements allowed us to detect the RM effect both directly as the distortion of the spectral lines in the planet shadow as well as in the RVs. From this, we measured a projected spin-orbit angle for the host star of $184 \pm 3°$. While this would suggest that the orbit of the planet is not only retrograde, but completely anti-aligned, the rotation period we measured from the TESS light curves suggests that the obliquity is $104 \pm 2°$, meaning that the orbit is actually polar.

Acknowledgements. We thank the anonymous referee for comments and suggestions which improved the manuscript. Based on observations collected at the European Organisation for Astronomical Research in the Southern Hemisphere under ESO programme 106.21TJ.001. We acknowledge the use of public TESS data from pipelines at the TESS Science Office and at the TESS Science Processing Operations Center. Resources supporting this work were provided by the NASA High-End Computing (HEC) Program through the NASA Advanced Supercomputing (NAS) Division at Ames Research Center for the production of

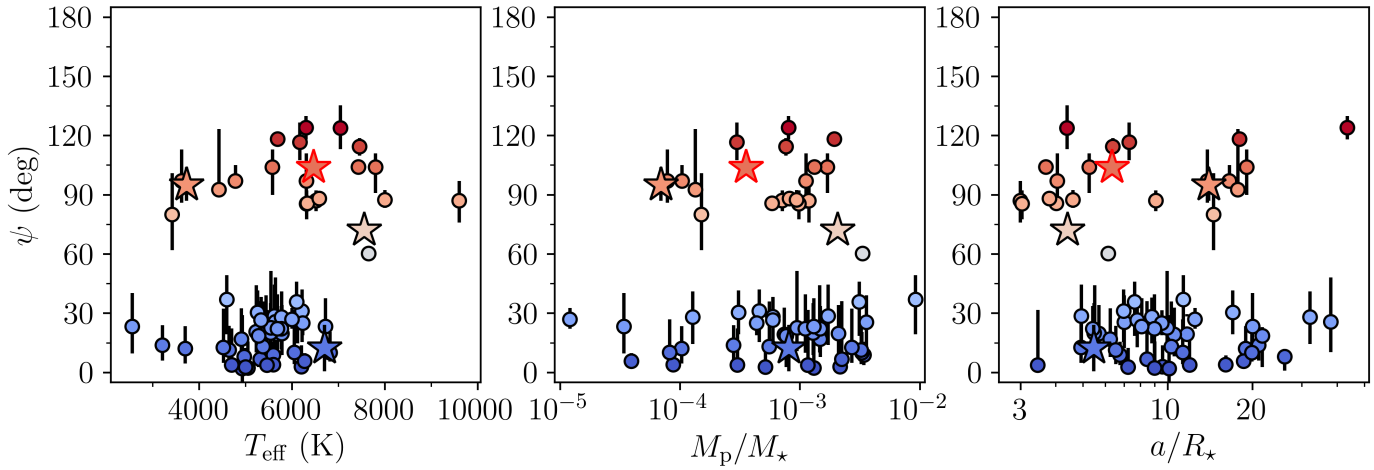

Fig. 8. Preponderance of perpendicular planets. Measurements of the 3D obliquity, ψ, from Albrecht et al. (2021) shown as circles with colour coding according to ψ. Recent ψ measurements not in Albrecht et al. (2021) are shown as stars, including TOI-640 (red outline). *Left*: ψ as a function of effective temperature. *Middle*: ψ as a function of planet-to-star mass ratio. *Right*: ψ as a function of orbital separation. It is worth noting that here we are only considering the results for ψ corresponding to i (and not $180° - i$).

the SPOC data products. Funding for the Stellar Astrophysics Centre is provided by The Danish National Research Foundation (Grant agreement no.: DNRF106). E.K. and S.A. acknowledge the support from the Danish Council for Independent Research through a grant, No.2032-00230B. The numerical results presented in this work were obtained at the Centre for Scientific Computing, Aarhus https://phys.au.dk/forskning/faciliteter/cscaa/. K.W.F.L. was supported by Deutsche Forschungsgemeinschaft grants RA714/14-1 within the DFG Schwerpunkt SPP 1992, Exploring the Diversity of Extrasolar Planets. C.M.P. and M.F. gratefully acknowledge the support of the Swedish National Space Agency (DNR 65/19, 177/19, 174/18, 2020-00104). This work is partly supported by JSPS KAKENHI Grant Number JP18H05439 and JST CREST Grant Number JPMJCR1761. This research made use of Astropy (http://www.astropy.org), a community-developed core Python package for Astronomy (Astropy Collaboration 2013, 2018, 2022). This research made use of matplotlib (Hunter 2007). This research made use of TESScut (Brasseur et al. 2019). This research made use of astroplan (Morris et al. 2018). This research made use of SciPy (Virtanen et al. 2020). This research made use of corner (Foreman-Mackey 2016). This research made use of statsmodels (Seabold & Perktold 2010).

References

Albrecht, S., Reffert, S., Snellen, I., Quirrenbach, A., & Mitchell, D. S. 2007, A&A, 474, 565
Albrecht, S., Setiawan, J., Torres, G., Fabrycky, D. C., & Winn, J. N. 2013a, ApJ, 767, 32
Albrecht, S., Winn, J. N., Marcy, G. W., et al. 2013b, ApJ, 771, 11
Albrecht, S. H., Marcussen, M. L., Winn, J. N., Dawson, R. I., & Knudstrup, E. 2021, ApJ, 916, L1
Albrecht, S. H., Dawson, R. I., & Winn, J. N. 2022, PASP, 134, 082001
Anderson, K. R., Winn, J. N., & Penev, K. 2021, ApJ, 914, 56
Astropy Collaboration (Robitaille, T. P., et al.) 2013, A&A, 558, A33
Astropy Collaboration (Price-Whelan, A. M., et al.) 2018, AJ, 156, 123
Astropy Collaboration (Price-Whelan, A. M., et al.) 2022, ApJ, 935, 167
Bakos, G. Á., Torres, G., Pál, A., et al. 2010, ApJ, 710, 1724
Beck, J. G., & Giles, P. 2005, ApJ, 621, L153
Brasseur, C. E., Phillip, C., Fleming, S. W., Mullally, S. E., & White, R. L. 2019, Astrophysics Source Code Library [record ascl:1905.007]
Brown, D. J. A. 2014, MNRAS, 442, 1844
Bruntt, H., Bedding, T. R., Quirion, P. O., et al. 2010, MNRAS, 405, 1907
Cegla, H. M., Lovis, C., Bourrier, V., et al. 2016, A&A, 588, A127
Claret, A. 2018, A&A, 618, A20
Claret, A., Hauschildt, P. H., & Witte, S. 2013, A&A, 552, A16
Cochran, W. D., Redfield, S., Endl, M., & Cochran, A. L. 2008, ApJ, 683, L59
Doyle, A. P., Davies, G. R., Smalley, B., Chaplin, W. J., & Elsworth, Y. 2014, MNRAS, 444, 3592
Fabrycky, D., & Tremaine, S. 2007, ApJ, 669, 1298
Fabrycky, D. C., & Winn, J. N. 2009, ApJ, 696, 1230
Foreman-Mackey, D. 2016, J. Open Source Softw., 1, 24
Foreman-Mackey, D., Hogg, D. W., Lang, D., & Goodman, J. 2013, PASP, 125, 306
Foreman-Mackey, D., Agol, E., Angus, R., et al. 2017, https://zenodo.org/record/806847
Foucart, F., & Lai, D. 2011, MNRAS, 412, 2799
Hirano, T., Suto, Y., Winn, J. N., et al. 2011, ApJ, 742, 69
Hooton, M. J., Hoyer, S., Kitzmann, D., et al. 2022, A&A, 658, A75
Hunter, J. D. 2007, Comput. Sci. Eng., 9, 90
Johnson, M. C., Cochran, W. D., Collier Cameron, A., & Bayliss, D. 2015, ApJ, 810, L23
Knudstrup, E., & Albrecht, S. H. 2022, A&A, 660, A99
Knudstrup, E., Serrano, L. M., Gandolfi, D., et al. 2022, A&A, 667, A22
Kreidberg, L. 2015, PASP, 127, 1161
Lai, D. 2012, MNRAS, 423, 486
Lai, D., Foucart, F., & Lin, D. N. C. 2011, MNRAS, 412, 2790
Lightkurve Collaboration (Cardoso, J. V. d. M., et al.) 2018, Astrophysics Source Code Library [record ascl:1812.013]
Lomb, N. R. 1976, Ap&SS, 39, 447
Louden, E. M., Winn, J. N., Petigura, E. A., et al. 2021, AJ, 161, 68
Lovis, C., & Pepe, F. 2007, A&A, 468, 1115
Masuda, K., & Winn, J. N. 2020, AJ, 159, 81
Maxted, P. F. L., Serenelli, A. M., & Southworth, J. 2015, A&A, 577, A90
Mayor, M., & Queloz, D. 1995, Nature, 378, 355
Mayor, M., Pepe, F., Queloz, D., et al. 2003, The Messenger, 114, 20
McQuillan, A., Aigrain, S., & Mazeh, T. 2013, MNRAS, 432, 1203
Morris, B. M., Tollerud, E., Sipocz, B., et al. 2018, Astrophysics Source Code Library [record ascl:1802.009]
Petrovich, C., Muñoz, D. J., Kratter, K. M., & Malhotra, R. 2020, ApJ, 902, L5
Ricker, G. R., Winn, J. N., Vanderspek, R., et al. 2015, J. Astron. Teles. Instrum. Syst., 1, 014003
Rodriguez, J. E., Quinn, S. N., Zhou, G., et al. 2021, AJ, 161, 194
Rogers, T. M., & Lin, D. N. C. 2013, ApJ, 769, L10
Romanova, M. M., Koldoba, A. V., Ustyugova, G. V., et al. 2021, MNRAS, 506, 372
Savitzky, A., & Golay, M. J. E. 1964, Anal. Chem., 36, 1627
Scargle, J. D. 1982, ApJ, 263, 835
Schlaufman, K. C. 2010, ApJ, 719, 602
Seabold, S., & Perktold, J. 2010, Proc. 9th Python in Science Conference
Southworth, J. 2011, MNRAS, 417, 2166
Stefánsson, G., Mahadevan, S., Petrovich, C., et al. 2022, ApJ, 931, L15
Stephan, A. P., Wang, J., Cauley, P. W., et al. 2022, ApJ, 931, 111
Szabó, G. M., Pál, A., Derekas, A., et al. 2012, MNRAS, 421, L122
Tabernero, H. M., Zapatero Osorio, M. R., Allende Prieto, C., et al. 2022, MNRAS, 515, 1247
Vick, M., Su, Y., & Lai, D. 2023, ApJ, 943, L13
Virtanen, P., Gommers, R., Oliphant, T. E., et al. 2020, Nat. Methods, 17, 261
Watanabe, N., Narita, N., & Johnson, M. C. 2020, PASJ, 72, 19
Watanabe, N., Narita, N., Palle, E., et al. 2022, MNRAS, 512, 4404
Winn, J. N., Fabrycky, D., Albrecht, S., & Johnson, J. A. 2010, ApJ, 718, L145
Wolszczan, A., & Frail, D. A. 1992, Nature, 355, 145

Yee, S. W., Winn, J. N., Hartman, J. D., et al. 2023, ApJS, 265, 1
Zahn, J. P. 1977, A&A, 57, 383

[1] Stellar Astrophysics Centre, Department of Physics and Astronomy, Aarhus University, Ny Munkegade 120, 8000 Aarhus C, Denmark
e-mail: emil@phys.au.dk
[2] Dipartimento di Fisica, Università degli Studi di Torino, via Pietro Giuria 1, 10125 Torino, Italy
[3] Thüringer Landessternwarte Tautenburg, Sternwarte 5, 07778 Tautenburg, Germany
[4] Division of Geological and Planetary Sciences, 1200 E California Blvd, Pasadena, CA, 91125, USA
[5] Department of Astronomy, California Institute of Technology, Pasadena, CA 91125, USA
[6] Astronomy Department and Van Vleck Observatory, Wesleyan University, Middletown, CT 06459, USA
[7] Astrobiology Center, 2-21-1 Osawa, Mitaka, Tokyo 181-8588, Japan
[8] National Astronomical Observatory of Japan, 2-21-1 Osawa, Mitaka, Tokyo 181-8588, Japan
[9] Institute of Planetary Research, German Aerospace Center (DLR), Rutherfordstrasse 2, 12489 Berlin, Germany
[10] Center for Planetary Systems Habitability and McDonald Observatory, The University of Texas at Austin, Austin Texas USA 78712, USA
[11] Instituto de Astrofísica de Canarias (IAC), 38200 La Laguna, Tenerife, Spain
[12] Departamento de Astrofísica, Universidad de La Laguna (ULL), 38206 La Laguna, Tenerife, Spain
[13] Leiden Observatory, PO Box 9513, 2300 RA Leiden, The Netherlands
[14] Department of Space, Earth and Environment, Chalmers University of Technology, Onsala Space Observatory, 439 92 Onsala, Sweden
[15] Department of Astronomy, The Graduate University for Advanced Studies (SOKENDAI), 2-21-1 Osawa, Mitaka, Tokyo, Japan
[16] Department of Astronomy & Astrophysics, University of Chicago, Chicago, IL 60637, USA
[17] Komaba Institute for Science, The University of Tokyo, 3-8-1 Komaba, Meguro, Tokyo 153-8902, Japan
[18] Mullard Space Science Laboratory, University College London, Holmbury St Mary, Dorking, Surrey RH5 6NT, UK

Appendix A: Additional tables and figures

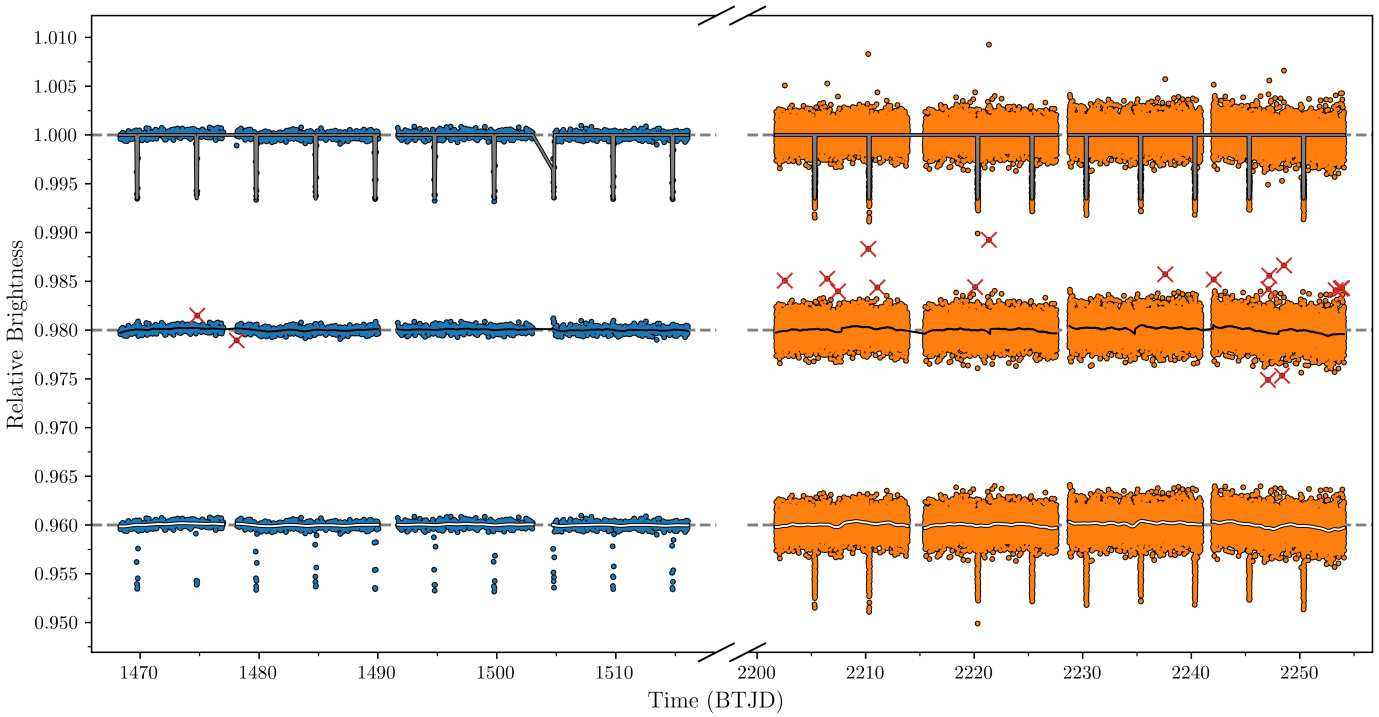

Fig. A.1. TESS photometry of TOI-640. TESS photometry of TOI-640 with Sectors 6 and 7 is shown in blue to the left and Sectors 33 and 34 in orange to the right. The light curves at the top have been corrected for scattered light. The grey curves show the best-fitting (determined iteratively) transit model. In the middle, we have subtracted this transit model. We used a Savitzky-Golay filter (black curve) to identify outliers, which are marked as red crosses. In the bottom, we have re-injected the transits into the light curves with the outliers removed. The white curves are the GPs we used to de-trend the data during our MCMC fit (see Section 3.1).

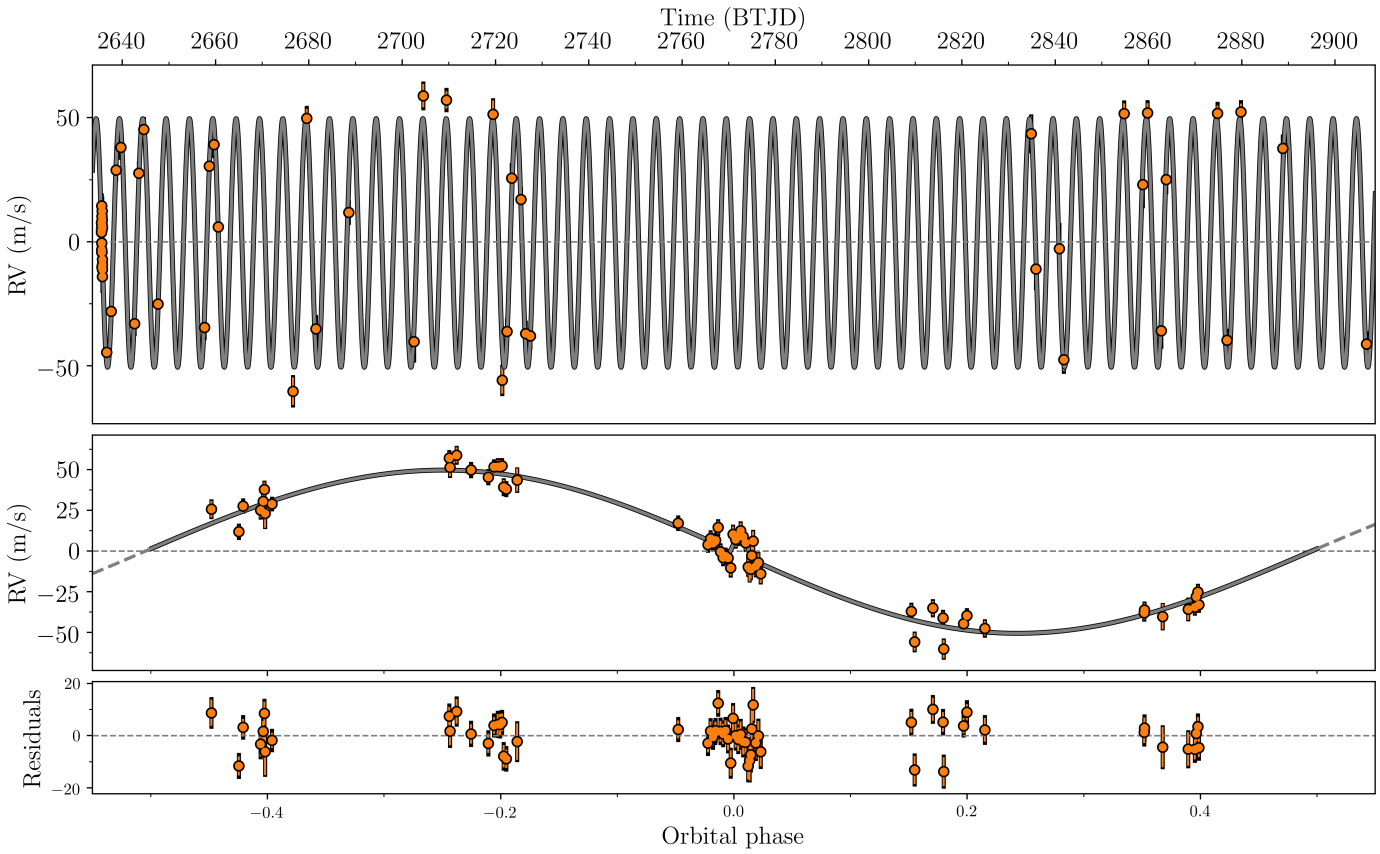

Fig. A.2. HARPS RVs. *Top:* HARPS RVs shown in orange with the best-fitting model overplotted in grey. *Middle:* HARPS RVs phase folded to the period of the planet for the values in Table 2. *Bottom:* Residuals after subtracting the Keplerian orbit and the RM effect.

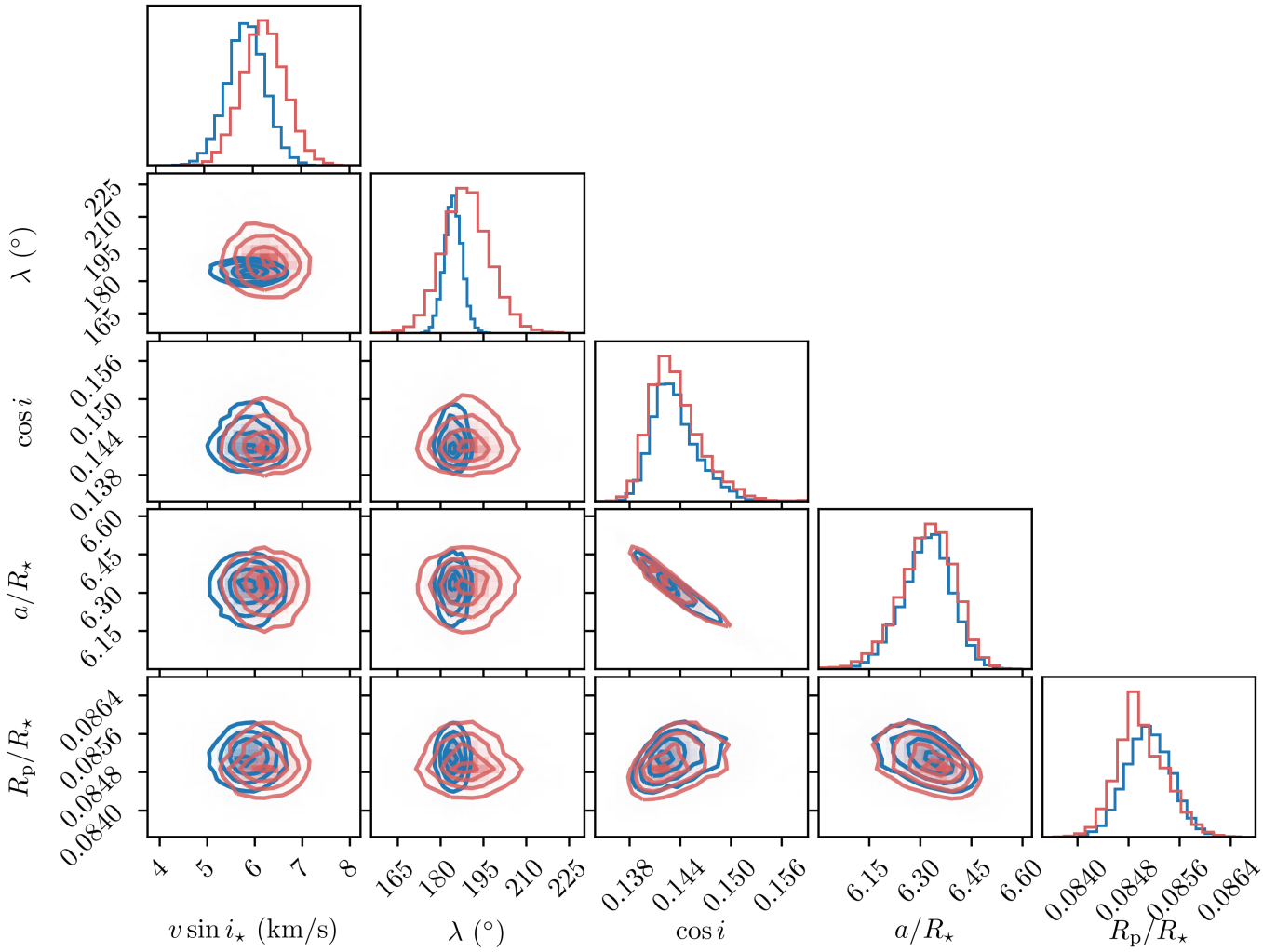

Fig. A.3. Correlation plots. Here we show the correlation between some of the stepping parameters from our MCMC (Section 3.1). Blue is from our run using the RVs as input for the RM effect, and red is using the shadow.

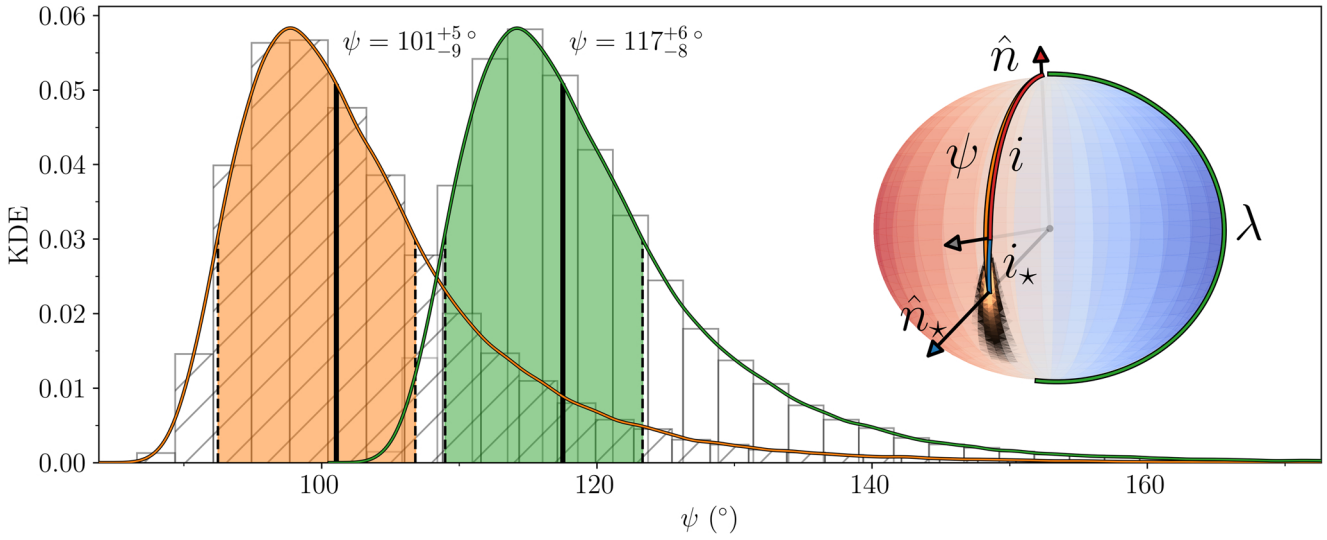

Fig. A.4. Spin-orbit angle distributions. The histograms are the distributions for ψ calculated from the relation in Louden et al. (2021), otherwise the meaning is the same as in Fig. 5.

Table A.1. HARPS transit RVs.

Time BJD_{TDB}	RV m s^{-1}	σ(RV) m s^{-1}	Exp. time s	SNR at 550 nm
2459635.51756438	40528.65	3.54	900	52.7
2459635.52844228	40532.54	3.69	900	50.2
2459635.53900864	40529.57	3.53	900	52.4
2459635.54967985	40531.40	3.43	900	54.3
2459635.56055881	40539.26	3.82	900	49.8
2459635.57133384	40524.30	4.01	900	48.2
2459635.58221429	40520.64	3.85	900	50.6
2459635.59267602	40521.66	4.00	900	49.2
2459635.60365925	40520.56	4.38	900	45.7
2459635.61443404	40514.51	4.86	900	41.5
2459635.62510594	40535.13	4.78	900	42.4
2459635.63598431	40531.87	4.57	900	44.4
2459635.64675899	40533.44	4.54	900	45.0
2459635.65732614	40537.21	4.87	900	42.2
2459635.66841376	40533.63	4.85	900	42.8
2459635.67898046	40529.91	4.58	900	45.2
2459635.68975559	40515.10	5.12	900	41.2
2459635.70063547	40513.60	5.81	900	37.0
2459635.71140933	40530.85	6.05	900	36.1
2459635.72228850	40515.54	5.94	900	36.9
2459635.73295947	40517.61	5.65	900	38.7
2459635.74373448	40510.81	5.62	900	39.1

The time stamps, RVs and associated errors, exposure times, and S/Ns for our HARPS observations on the transit night.

Table A.2. HARPS RVs.

Time BJD_{TDB}	RV m s^{-1}	σ(RV) m s^{-1}	Exp. time s	SNR at 550 nm
2459636.61429745	40480.25	2.98	1500	64.5
2459637.61272941	40496.75	3.20	1500	60.7
2459638.65059912	40553.67	2.90	1500	68.3
2459639.65598973	40562.80	3.55	1500	55.8
2459642.62712950	40491.86	3.61	1500	55.1
2459643.53042388	40552.43	3.23	1500	58.0
2459644.58214205	40570.11	3.68	1500	53.1
2459647.62659055	40499.68	3.79	1200	53.5
2459657.62127673	40490.31	3.89	1200	52.2
2459658.62766323	40555.27	3.95	1200	51.4
2459659.65953279	40564.03	4.29	1200	48.6
2459660.56634930	40530.77	3.34	1200	59.4
2459676.55929847	40464.58	5.58	1400	36.7
2459679.53476551	40574.59	3.69	1400	53.0
2459681.51615428	40489.74	4.41	1200	45.3
2459688.54613223	40536.66	3.67	1400	54.9
2459702.51767879	40484.57	7.71	1400	28.1
2459704.49113530	40583.64	4.72	1200	43.2
2459709.46414553	40581.93	3.51	1500	55.8
2459719.47467143	40576.20	5.52	1500	37.6
2459721.46803448	40469.00	5.36	1500	38.1
2459722.45452427	40488.65	3.97	1500	50.7
2459723.45482634	40550.48	5.03	1500	41.6
2459725.45734693	40541.89	3.42	1500	58.5
2459726.45743072	40487.81	3.99	1500	50.4
2459727.45664837	40486.89	4.16	1500	48.6
2459834.84967236	40568.37	7.04	1200	29.2
2459835.84688757	40513.81	7.70	1200	27.6
2459840.85990011	40522.06	9.83	1200	22.5
2459841.86062937	40477.29	4.58	1200	42.3
2459854.79154962	40576.47	4.13	1200	46.3
2459858.78710518	40547.88	8.92	1200	24.2
2459859.78571868	40576.71	3.91	1200	49.1
2459862.74740732	40488.98	6.46	1200	32.2
2459863.77184520	40549.89	4.76	1200	41.5
2459874.78085079	40576.56	3.16	1200	58.0
2459876.80989269	40485.16	3.17	1200	57.1
2459879.81844207	40577.14	3.36	1200	54.5
2459888.80667830	40562.48	4.45	1200	42.3
2459906.72984965	40483.65	3.76	1200	49.3

The time stamps, RVs and associated errors, exposure times, and S/Ns for our HARPS monitoring observations carried out from 2022 February 26 to November 23.

Table A.3. Additional parameters.

Parameter	Name	Prior	RV Value	Shadow Value
	Stepping parameters			
$\log A_1$	GP amplitude TESS 2 min.	$\mathcal{U}$	-8.50 ± 0.09	$-8.50^{+0.09}_{-0.10}$
$\log \tau_1$	GP time scale TESS 2 min. (log days)	$\mathcal{U}$	-0.20 ± 0.15	$-0.19^{+0.14}_{-0.18}$
$\log A_2$	GP amplitude TESS 30 min.	$\mathcal{U}$	$-9.41^{+0.12}_{-0.13}$	-9.41 ± 0.13
$\log \tau_2$	GP time scale TESS 30 min. (log days)	$\mathcal{U}$	0.0 ± 0.3	0.0 ± 0.4
$q_1 + q_2$	Sum of limb-darkening coefficients TESS	$\mathcal{N}(0.527,0.1)$	0.496 ± 0.019	$0.496^{+0.021}_{-0.019}$
$q_1 + q_2$	Sum of limb-darkening coefficients HARPS	$\mathcal{N}(0.6974,0.1)$	$0.75^{+0.09}_{-0.08}$	0.71 ± 0.09
	Fixed parameters			
$q_1 - q_2$	Difference of limb-darkening coefficients TESS	$\mathcal{F}(-0.1028)$		
$q_1 - q_2$	Difference of limb-darkening coefficients HARPS	$\mathcal{F}(0.2400)$		
	Derived parameters			
q_1	Linear limb-darkening coefficient TESS		0.197 ± 0.010	$0.197^{+0.011}_{-0.010}$
q_1	Quadratic limb-darkening coefficient TESS		0.300 ± 0.010	$0.300^{+0.011}_{-0.010}$
q_1	Linear limb-darkening coefficient HARPS		0.50 ± 0.04	0.40 ± 0.05
q_2	Quadratic limb-darkening coefficient HARPS		0.26 ± 0.04	0.305 ± 0.045

GP hyper parameters and limb-darkening coefficients from our MCMCs. Same as in Table 2.